2024 IEEE 74th Electronic Components and Technology Conference (ECTC) | 979-8-3503-7598-5/24/$31.00 ©2024 IEEE | DOI: 10.1109/ECTC51529.2024.00393

Additively Manufactured RF Interconnects for D-Band/sub-THz Applications

Genaro Soto-Valle, Nikolas Roeske, Kexin Hu, Yaw A. Mensah, John D. Cressler, Manos M. Tentzeris
School of Electrical and Computer Engineering
Georgia Institute of Technology
Atlanta, GA, USA
genarosva@gatech.edu

***Abstract*—The rapid development in micro additive manufacturing (μAM) of metals has the potential to enable a new generation of miniaturized devices capable of achieving complex 3D geometries that can be integrated with other conventional manufacturing methods, paving the way for a new range of applications across multiple fields. In this work, a novel metal micro additive manufacturing method is utilized to demonstrate for the first time the fabrication of micro-scale interconnect structures capable of operating up to 150 GHz. The μAM process consists of a localized electrodeposition process that utilizes an atomic force microscope cantilever tip, which can achieve printing resolutions in the order of microns. The interconnect structures were 3D printed and aligned to a CPW transmission line on a high-resistivity 15-by-15 mm Si substrate, which was prepared utilizing a photolithography process. This fabrication approach has the potential to enable the next generation of additively manufactured devices targeted for sub-THz applications with stringent requirements of good resolution and high conductivity.**

***Index Terms*—interconnects, wire bonding, micro additive manufacturing, millimeter wave, sub-THz, metal 3D printing**

I. Introduction

In recent years, additive manufacturing (AM) technologies have been demonstrated to be significantly beneficial for a wide variety of sectors. In the microscale realm, recent efforts have realized novel technologies capable of manufacturing microarchitectures, motivated by the push toward miniaturized applications in microelectronics, optics, microrobotics, small-scale sensors, among others. Particularly for metals, the more mature techniques such as direct metal laser sintering (DMLS) or electron beam melting (EBM) are expensive and require multiple pre and post processing steps that make the printing process not as accessible and limited for multiple applications [1], [2]. For instance, both EBM and DMLS are powder-based techniques, meaning they require a powdered metal bed to enable the sintering process. Although they can achieve complex geometries with resolutions of 20 – 50 μm and have good surface quality, the powder bed requirement makes it difficult to integrate with the fabrication processes of integrated circuits (IC) devices, as it can cause contamination and produce a much more complicated process flow. Moreover, both of these devices are notoriously difficult to purchase and operate given their high-power requirement, often requiring dedicated skilled operators, supporting equipment, and bulky powder management systems, causing them to have slow iteration processes in order to achieve one functional part [3].

Nevertheless, in the past few years, a novel metal micro additive manufacturing (μAM) technique based on localized electrodeposition has been reported [2], [4], [5]. The electrochemical process offers inherent benefits compared to other metal printing techniques, including minimal waste generation; not requiring post-processing steps; it can achieve overhang structures without the need for supports; and is fully compatible with integrated-circuit (IC) packaging and PCB production processes [6]. Previous works have reported the fabrication of several different structures with the aforementioned technique, with geometries ranging from pillars [7], helixes [8], hollow microneedles [9], and even a replica of the David statue [5]. Because it is based on a standard electrodeposition process, the technique is compatible with any metal that can be electroplated. The work in [6] has demonstrated to print structures made of pure gold, achieving a conductivity value 2.5 times higher than the bulk conductivity.

The field of millimeter wave (mmWave) technology has been exponentially growing in the last decade. Nowadays, the mobile communication industry has started the commercialization and deployment of 5G networks, allowing high data-rate communication and enhancing technologies such as Internet of Things, self-driving vehicles, and large-scale sensor networks [10], [11]. As the 5G becomes more standardized, researchers have begun to investigate and develop future 6G communication networks that would allow operation above 100 GHz and up to THz frequencies [11], enabling ultra-reliable low-latency communications, as well as holographic and tactile communications [11], [12]. The path toward 6G technologies requires RF devices that are reliable, easily scalable, affordable, and efficient in their fabrication process. In this regard, AM technologies are a desired solution because they address those requirements.

Previous works have demonstrated the fabrication of several RF modules capable of operating in W-band (75 GHz – 110 GHz) by inkjet printing [13], [14] and aerosol-jet printing [15], [16]. Other works have even reported the fabrication of antenna modules operating up to D-band (110 GHz – 170 GHz) by DMLS process as well as dielectric printing followed by a metal plating process, as summarized in [17]. For inkjet and aerosol-jet printing, reaching higher frequency bands is a great challenge given the inherent printing resolution of these systems. Moreover, they cannot achieve complex 3D geometries. Hence, there is still a need for a better and

2377-5726/24/$31.00 ©2024 IEEE
DOI 10.1109/ECTC51529.2024.00393

Authorized licensed use limited to: Georgia Institute of Technology. Downloaded on August 12,2024 at 23:18:23 UTC from IEEE Xplore. Restrictions apply.

more efficient way of AM technique that overcomes these limitations in order to enable the production of future 6G/sub-THz RF modules.

The electrodeposition-based µAM technique offers tremendous potential for use in mmWave applications, as it overcomes the limitations of the aforementioned AM techniques; the conductivity values, the resolution limit, and the geometries it can achieve are significantly better. As of today, only one work has utilized this µAM technique to fabricate RF devices, consisting of a traveling wave tube that operates in the 60GHz – 80 GHz band [18]. With the printing resolution of this technique, the design of mmWave modules operating at frequencies in the order of hundreds of GHz can be envisioned. Therefore, in this work, the fabrication of interconnect structures operating up to 140 GHz is demonstrated for the first time. The electrodeposition-based µAM technique utilized in this work has the potential to enable a multitude of on-chip architectures for 5G/6G applications, including complex 3D overhanging structures for interconnects and antenna architectures. Moreover, it can be easily integrated with other semiconductor fabrication processes, producing a simpler workflow that is reliable and efficient.

II. Metal Micro 3D Printing Process

The µAM process utilized to fabricate the interconnect structures was realized utilizing the CERES system (Exaddon AG, Zürich, Switzerland), which consists of a localized electrodeposition process that utilizes an atomic force microscope (AFM) cantilever with an integrated microfluidic channel connected to a reservoir where the electrolyte solution is deposited [4], [5]. The cantilever tip has a nozzle with a diameter of 300 nm through which the solution is ejected, providing the metal ions required to support the electrochemical reaction. In this work, copper was utilized as the printing material, and the electrolyte ink was comprised of a 0.5 M copper sulfate ($CuSO_4$) solution mixed in sulfuric acid (H_2SO_4) and hydrochloric acid (HCl) [19].

Similarly to a standard electrodeposition technique, the printing process occurs in a three-electrode cell that consists of a working electrode (WE), a reference electrode (RE), and a counter electrode (CE). Therefore, the cantilever tip, as well as the printing substrate, have to be immersed in a supporting buffer solution during the full operation. The buffer solution, contained in the printing chamber, is a mixture of sulfuric acid (0.5 mM) and hydrochloric acid (54 mM) in water [19]. The acid solution is compatible with most materials utilized in semiconductor fabrication, and it does not affect the overall device fabrication process. A user-defined potential is applied on the working electrode, and the ejection of the copper solution from the tip nozzle into the cell is controlled by applying air pressure at the tip reservoir. The metal reduction reaction occurs when the ions establish contact with the WE surface (i.e. the substrate), causing the copper to solidify and grow following the tip movement in $x-$, $y-$ or $z-$axis. A diagram of the printing operation is presented in Fig. 1.

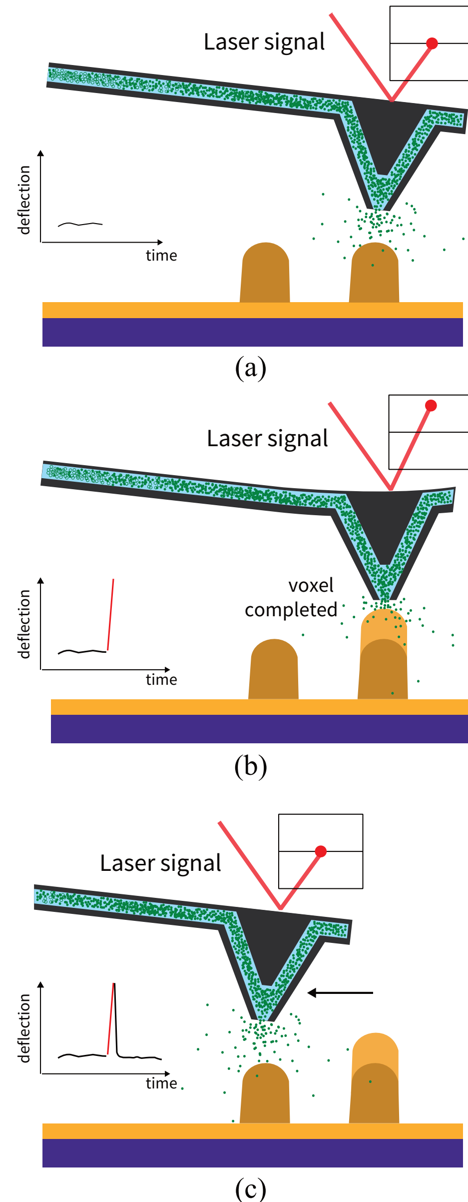

Fig. 1. Schematic of the metal micro 3D printing process, showing the cantilever tip with the microfluidic channel filled with the copper solution. The laser beam points at the back of the tip to detect deflection movement during the voxel growth. (a) The tip ejects material on the second printing layer. (b) Once the voxel has formed, the tip deflects and the laser beam reflection moves, causing a peak in the laser signal. This triggers the signal to move to the next voxel position. (c) The printing process continues and repeats. Adapted from [2].

The cantilever movement is continuously monitored with an optical beam deflection system to retrieve feedback on the solidification process, as shown in Fig. 1. The printing process is initialized once the cantilever tip has established a vertical distance from the substrate surface between 0.5 µm and 2 µm, as established by the user. This height corresponds to the voxel (volumetric pixel) height. The *voxel* is the building block utilized by the printer system to build the desired structure. As

Authorized licensed use limited to: Georgia Institute of Technology. Downloaded on August 12,2024 at 23:18:23 UTC from IEEE Xplore. Restrictions apply.

the metal ions released from the cantilever tip aperture reach the working electrode, solid material grows vertically until it establishes contact with the tip nozzle, causing a deflection on the tip that is detected by the laser beam. This means that the voxel is complete. As mentioned, the cantilever deflection is continuously tracked, and once the deflection magnitude surpasses a specific threshold, the tip moves to the next voxel position and repeats the process until the full structure has been seamlessly formed in a layer-by-layer fashion. The voxel diameter in the $xy-$plane can be controlled by modifying the amount of pressure that is applied on the tip reservoir, which also affects the printing speed because the effective amount of material flow changes: the higher the material flow the faster the printing speed [5]. Therefore, the resolution in $x–y$ is also determined by the voxel diameter, which can range from 1.7 µm to 7 µm with a pressure range of 10 mbar to 500 mbar, respectively [4]. By tracking the cantilever deflection, the CERES system is capable of providing real-time measurements of the voxel printing speed.

III. Device Fabrication

As described in the previous section, the substrate effectively acts as the working electrode required to support the electrochemical process. In other words, the substrate surface must be conductive to successfully promote the ion reduction process and build solid copper. Therefore, for integrated circuit applications, a pattern has to be fabricated on the substrate prior to starting the metal micro 3D printing process.

The overall fabrication process was comprised of two parts. First, the substrate preparation utilizing a photolithography process was necessary to achieve feature sizes as small as 10 µm and below. Secondly, the fabrication of the interconnect structures was realized by micro 3D printing on the CERES system. This section describes in more detail each of these fabrication parts.

A. Substrate Patterning of CPW Structures

A conductive pattern is required to establish a proper electrical connection between the initial printing position and the working electrode within the electrochemical cell. Moreover, a correct RF design is also necessary for the excitation and characterization of the interconnect structures. Therefore, a pattern consisting of coplanar waveguide (CPW) structures was designed and fabricated on a silicon (Si) substrate. The CPW and the interconnect structures were targeted for operation up to 150 GHz. A complete overview of the final pattern design is presented in Fig. 2.

The printing chamber of the CERES system can hold squared substrates of two sizes: 15 mm by 15 mm and 25 mm by 25 mm. In this work, a 15mm–by–15mm substrate was selected. As shown in Fig. 2, the CPW structures are located in the center of the substrate. The actual printing area for a 15mm-by–15mm substrate has a diameter of 8 mm, established by the system design as that is the area that ensures a safe cantilever movement. The printing area can be upgraded to a diameter of 16mm when a 25mm–by–25mm substrate is

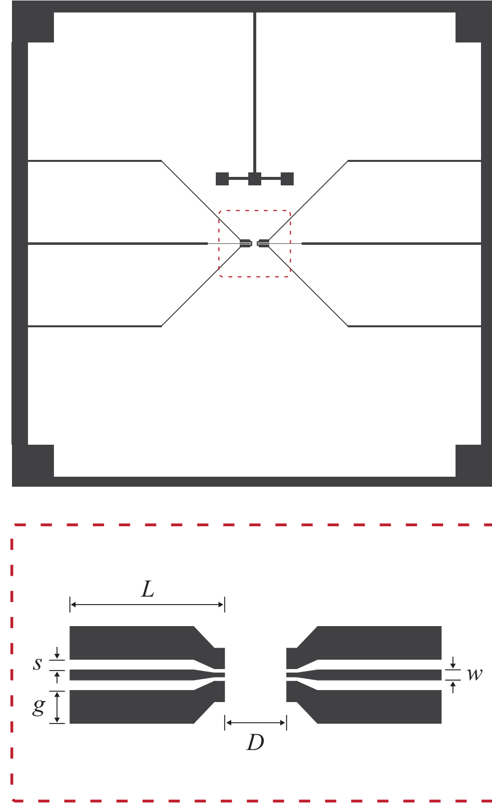

Fig. 2. Conductive pattern fabricated on Si utilized as the printing substrate for the micro 3D printing process of the interconnects. The overall substrate size is 15mm × 15 mm. The dotted square at the center of the substrate is expanded at the bottom diagram, where the CPW geometry is presented. The corresponding dimensions are $L = 375$µm, $D = 150$µm, $s = w = 25$µm, and $g = 80$µm. On the inner side, s, w and g are 10 µm, 10 µm, and 50 µm, respectively.

utilized. The CPW structures are separated by a gap where the interconnects will be located, corresponding to a distance (D) of 150 µm. The width of the signal line (w) and the spacing (s) between the signal line and the ground traces are both 25 µm to match an impedance of 50 Ω. The ground lines have a width (g) of 80 µm. The inner sides of the CPW structures are tapered down to a CPW line with $w = s = 10$µm and $g = 50$µm. Conductive traces were connected from the outer part of the CPW structures to a conductive frame at the edges of the square substrate to establish an electrical connection with the working electrode and support the micro 3D printing process. The reason for adding the conducive frame is because the µAM system makes contact with the substrate at the four corners of the substrate, hence, four squared pads were placed on each corner. Conductor pads were also added next to the CPW structures and connected to the conductive frame in order to provide a printing area to facilitate the alignment procedure, explained in more detail in the following section.

The pattern was fabricated by a bi-layer lift-off process on a 4-in high-resistivity Si wafer. The process consisted of a photolithography process followed by a metal deposition via

Authorized licensed use limited to: Georgia Institute of Technology. Downloaded on August 12,2024 at 23:18:23 UTC from IEEE Xplore. Restrictions apply.

thermal evaporation. The first step of the fabrication was to spin coat a layer of LOR 10B resist followed by a second layer of positive SC1827 photoresist. The use of two resist layers was selected to achieve the lift-off process with a positive photoresist, reducing the time of the UV exposure process. A maskless aligner tool (Heidelberg, MLA 150) was utilized to expose the photoresist to UV and create the pattern from Fig. 2. Afterward, the exposed photoresist was developed and then the wafer was cleaned by a plasma descum process (plasma cleaning) to remove photoresist residues from the developed areas and promote metal adhesion. Then, a 20-nm layer of titanium followed by a 1-µm layer of copper was deposited by thermal evaporation, to finally proceed with the lift-off step by submerging the wafer in acetone for 5 hours. The titanium thin layer was added to also promote the surface adhesion between copper and the silicon substrate. The 4-inch Si wafer was diced into 15-by-15mm substrates containing the same pattern as Fig. 2, completing the substrate preparation before proceeding to the micro 3D printing of the interconnects.

B. Alignment and 3D Printing of Interconnects

Once the pattern fabrication process was finalized, the 15-by-15 mm samples were loaded into the printing chamber containing the buffer solution to proceed with the 3D printing of the interconnect structures. As mentioned in Section II, the object is constructed in a voxel-by-voxel fashion, one layer at a time. The print files for the µAM system consist of a comma-separated values (CSV) file containing a four-column list; the fist three columns corresponding to each of the voxel's positions in 3-dimensional space (X, Y, Z), and the fourth column corresponding to the applied pressure for each voxel. In this work, the files were designed and generated by the CERES system's integrated print file generator [19], which contains a predefined set of basic geometries such as pillars and helical structures. Files can be generated using any custom script as long as the CSV file follows the aforementioned specifications.

The spacing between voxels is a crucial parameter for a successful print. If voxels are tightly spaced, voxel collisions can occur producing print failures. On the other hand, a large spacing can result in voxels that are not well merged together, causing structure irregularities and a degradation in electrical conductivity across the overall structure. Moreover, the thickness of the structure is directly related to the structure's sturdiness; the thicker the diameter of the interconnect, the more amount of force and stress it can withstand. Therefore, multiple iterations of the interconnect geometry were tested to ensure it can support itself and minimize printing failures. The selected geometry for the printed interconnect architecture is depicted in Fig. 3. The arch shape was selected after verifying that the printing sequence for that geometry was found to be optimal as the number of voxel collisions detected by the system was effectively zero. Moreover, this design did not require supporting structures because the radius of curvature was large enough to allow the arch structure to support itself without collapsing on itself. Different geometries, such as a rectangular bridge, were also tested but were challenging to achieve since they collapsed on themselves before completing the connection.

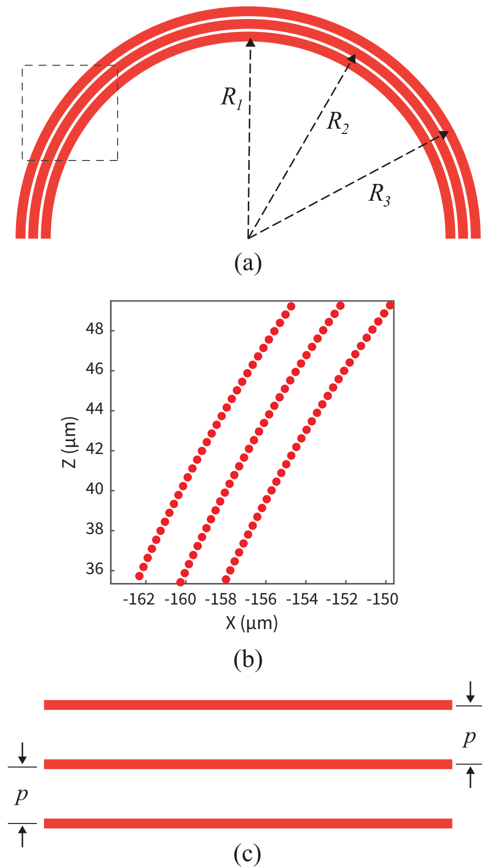

Fig. 3. Schematic of the interconnect geometry. (a) Side view of a single interconnect structure, consisting of three vertically stacked arches with radii $R_1 = 83$µm, $R_2 = 85$µm, and $R_3 = 87$µm. (b) Detailed view of a section of the interconnect highlighting the individual voxels. (c) Top view of the three interconnect structures separated by a gap of $p = 20$µm.

The voxel growth in the $x-y$ direction is mainly determined by the applied air pressure on the cantilever tip, whereas the growth in the z direction is specified by the $z-$layer height. Hence, the voxel spacing in $x - y$ can be different from the spacing in z direction, depending on the desired geometry. For this work, the selected geometry of a single interconnect consists of three arches vertically stacked and merged together to achieve a width equivalent to three voxels, making it thick enough to support its own weight. The geometry is observed in Fig. 3a, and a detailed view of each individual voxel is presented in Fig. 3b. The spacing between voxels was set to 0.5 µm along each individual arch and a 2 µm difference in radius, corresponding to $R_1 = 83$µm, $R_2 = 85$µm, and $R_3 = 87$µm, respectively. The applied pressure was set to 100 mbar, which lies within the system's recommended pressure range. At an applied pressure of 100 mbar, the typical voxel diameter ranges from 1.5 to 3 µm, so the total width is approximately 6 µm. From the top view shown in Fig. 3c, the three interconnect

Authorized licensed use limited to: Georgia Institute of Technology. Downloaded on August 12,2024 at 23:18:23 UTC from IEEE Xplore. Restrictions apply.

structures have a separation (p) of 20 µm to leave enough clearance for the alignment with the CPW lines that have a gap of 10 µm, as described in the previous section. Each of the individual interconnect structures contained 1603 voxels, adding up to a total of 4809 voxels for the three structures. The overall printing time for this design was 45 minutes, with an approximate printing speed of 500 ms per voxel at a pressure of 100 mbar.

Once the substrate was loaded into the printing chamber and before starting the 3D printing process, the interconnect structures needed to be aligned with the CPW traces. The CERES system has an integrated optical camera for this purpose. First, a calibration pillar was printed on the copper pads above close to the CPW lines to measure the system offset between the system printing position and the real printed position. Afterward, the measured offset is calibrated and the alignment procedure follows. A digital projection of the interconnect structures is shown on the system's screen and a manual alignment is performed until the projection coincides with the desired starting point on top of the CPW structures. If needed, the CERES system is also capable of sub-micron alignment accuracy by utilizing the cantilever tip as an AFM probe, generating a surface height map of the substrate.

IV. Device SEM Imaging and Measurements

After the printing process was completed, the fabricated samples were analyzed under a scanning electron microscope (SEM) from Hitachi (S-3700N). The results are presented in Fig. 4. As observed, the three interconnect structures were successfully printed and aligned on the CPW transmission lines. The measured length between the contact points on each side of the arch was 168.5 µm and the height from the base to the innermost arch was 81.25 µm, resulting in a difference of 1.5 µm and 1.75 µm, respectively. The vertical width corresponding to three voxels in diameter was 6.3 µm, whereas the horizontal diameter corresponding to a single voxel measured 2.9 µm. It can also be noted that the highest point of the arch located in the middle of the structure has a reduced diameter, both horizontally and vertically, of approximately 1 µm. This connection point was challenging to achieve in previous geometry iterations, as it was where the structure collapsed. However, for the selected geometry, the voxels are completely merged and the electrical connection is established. A mismatch in the alignment with respect to the CPW lines can be also observed in Fig. 4d and Fig. 4e. This offset caused the interconnect structure to be printed 2 µm away from the center of the CPW line on the right side and 3 µm away from the center on the left side, which corresponds to an angle misalignment of approximately 0.5 degrees. This alignment can be significantly improved by utilizing the system's feature for sub-micron alignment performed by using the cantilever tip in AFM mode to create a surface map of the printing area.

The performance of the fabricated device was measured utilizing a Cascade Microtech PM8 probe system with WR6 Infinity waveguide GSG probe tips with a 75-µm pitch. A 43.5-GHz PNA-X network analyzer (Agilent Technologies)

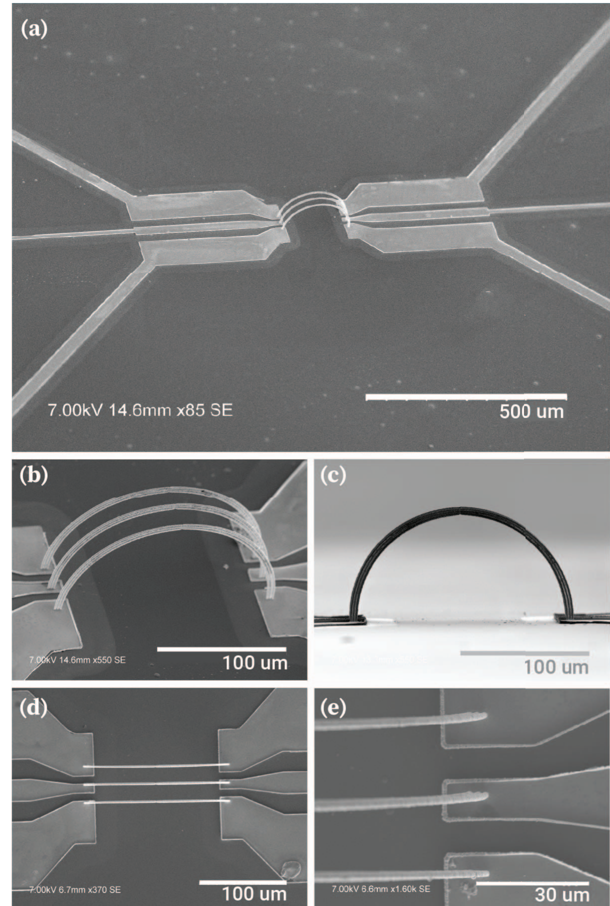

Fig. 4. Scanning electron microscope images of the 3D printed interconnect structures. (a) 45-degree view. (b) Higher magnification of interconnect section from (a). (c) Side view. (d) Top view. (e) Higher magnification from (d) focusing on the right-side connection with the CPW transmission lines.

connected to a millimeter wave VNA extender (OML, Inc.) was utilized to measure in the D-Band frequency range (110 GHz – 170 GHz). The lines connecting the end of the CPW lines to the edge of the substrate were mechanically detached in order to properly measure the device response.

The measured S21 parameter of the full device is shown in Fig. 5, as well as the simulation results modeled in ANSYS HFSS. The aforementioned offsets in dimensions between the fabricated and measured device were accounted and the model was adjusted to capture a more accurate performance of the device. As it is observed, the insertion loss of the device increases from 2.5 dB to 4.8 dB from 110 GHz to 140 GHz. The measured insertion loss matches the modeled performance up to 135 GHz and the loss becomes more pronounced above that frequency.

The observed losses can be attributed to an impedance mismatch between the CPW transmission line and the interconnect structure, which can be improved in future system iterations by implementing a stepped impedance-matching transformer as the one reported in [20] for a D-Band wire bond interconnects.

Authorized licensed use limited to: Georgia Institute of Technology. Downloaded on August 12,2024 at 23:18:23 UTC from IEEE Xplore. Restrictions apply.

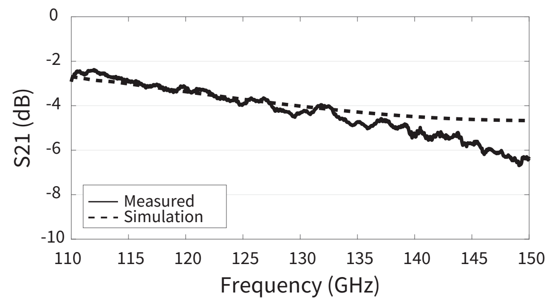

Fig. 5. Comparison of the insertion loss between the fabricated device and the corresponding simulation.

Other possible sources of loss are a decreased conductivity value for the 3D printed copper wire structures as well as radiation losses caused by the continuous curvature across the total arch geometry. A future design with straight-line paths instead of a continuous bend across the overall interconnect will be analyzed to minimize possible radiation losses. In addition, wires with thicker diameters would help achieve a better connection between the printed voxels, thus improving the overall conductivity and surface roughness.

V. Conclusions

In this paper, the fabrication of solid copper wire interconnects via an additive micromanufacturing process operating in the D-Band has been reported for the first time. The full fabrication process including the substrate patterning using photolithography methods and the metal micro 3D printing details has been thoroughly described. The system has demonstrated to realize the designed geometries with an accuracy in the order of 2 µm and can achieve alignment accuracy in the sub-micron scale. Moreover, the interconnects demonstrated to operate in the D-Band frequency range, as shown by the measurements up to 140 GHz. With improvements in matching and overall geometry, the fabrication approach presented here has the potential to reach higher operating frequencies. This electrodeposition-based micro 3D printing method is capable of realizing overhanging structures without the need for supporting structures, therefore significantly simplifying the fabrication of complex 3D architectures. In addition, it is compatible with a wide range of metals, so the electrical and mechanical properties of the printed structures can be adjusted depending on the metal of interest. This technology opens the way for novel on-chip architectures capable of combining conventional chip fabrication processes with additive manufacturing, enabling geometries that are not possible to achieve by a different means.

Acknowledgements

The authors would like to thank the personnel from the Georgia Tech's Institute for Electronics and Nanotechnology Cleanroom for all the support provided to realize this work, especially to Dr. Durga Gajula for his input on the lift-off process.

References

[1] M. Vaezi, H. Seitz, and S. Yang, "A review on 3d micro-additive manufacturing technologies," *The International Journal of Advanced Manufacturing Technology*, vol. 67, no. 5-8, pp. 1721–1754, 2013.

[2] L. Hirt, S. Ihle, Z. Pan, L. Dorwling-Carter, A. Reiser, J. M. Wheeler, R. Spolenak, J. Vörös, and T. Zambelli, "Template-free 3d microprinting of metals using a force-controlled nanopipette for layer-by-layer electrodeposition," *Advanced Materials*, vol. 28, no. 12, pp. 2311–2315, 2016.

[3] S. Legutko, "Additive techniques of manufacturing functional products from metal materials," *IOP Conference Series: Materials Science and Engineering*, vol. 393, p. 012003, 2018.

[4] G. Ercolano, T. Zambelli, C. van Nisselroy, D. Momotenko, J. Vörös, T. Merle, and W. W. Koelmans, "Multiscale additive manufacturing of metal microstructures," *Advanced Engineering Materials*, vol. 22, no. 2, 2019.

[5] G. Ercolano, C. van Nisselroy, T. Merle, J. Voros, D. Momotenko, W. W. Koelmans, and T. Zambelli, "Additive manufacturing of sub-micron to sub-mm metal structures with hollow afm cantilevers," *Micromachines*, vol. 11, no. 1, 2019.

[6] P. Schürch, D. Osenberg, P. Testa, G. Bürki, J. Schwiedrzik, J. Michler, and W. W. Koelmans, "Direct 3d microprinting of highly conductive gold structures via localized electrodeposition," *Materials Design*, vol. 227, 2023.

[7] R. Ramachandramoorthy, S. Kalácska, G. Poras, J. Schwiedrzik, T. E. J. Edwards, X. Maeder, T. Merle, G. Ercolano, W. W. Koelmans, and J. Michler, "Anomalous high strain rate compressive behavior of additively manufactured copper micropillars," *Applied Materials Today*, vol. 27, 2022.

[8] W. Ren, J. Xu, Z. Lian, X. Sun, Z. Xu, and H. Yu, "Localized electrodeposition micro additive manufacturing of pure copper microstructures," *International Journal of Extreme Manufacturing*, vol. 4, no. 1, 2021.

[9] R. Sachan, P. Schürch, P. Testa, E. Hepp, W. W. Koelmans, and R. J. Narayan, "Hollow copper microneedle made by local electrodeposition-based additive manufacturing," *MRS Advances*, vol. 6, no. 39-40, pp. 893–896, 2021.

[10] R. Dangi, P. Lalwani, G. Choudhary, I. You, and G. Pau, "Study and investigation on 5g technology: A systematic review," *Sensors*, vol. 22, no. 1, p. 26, 2022.

[11] S. Dang, O. Amin, B. Shihada, and M.-S. Alouini, "What should 6g be?" *Nature Electronics*, vol. 3, no. 1, pp. 20–29, 2020.

[12] W. Jiang, B. Han, M. A. Habibi, and H. D. Schotten, "The road towards 6g: A comprehensive survey," *IEEE Open Journal of the Communications Society*, vol. 2, pp. 334–366, 2021.

[13] B. Tehrani, B. Cook, J. Cooper, and M. Tentzeris, "Inkjet printing of a wideband, high gain mm-wave vivaldi antenna on a flexible organic substrate," in *2014 IEEE Antennas and Propagation Society International Symposium (APSURSI)*, 2014, pp. 320–321.

[14] J. Kimionis, S. Shahramian, Y. Baeyens, A. Singh, and M. M. Tentzeris, "Pushing inkjet printing to w-band: An all-printed 90-ghz beamforming array," in *2018 IEEE/MTT-S International Microwave Symposium - IMS*, 2018, pp. 63–66.

[15] M. T. Craton, X. Konstantinou, J. D. Albrecht, P. Chahal, and J. Papapolymerou, "Additive manufacturing of a w-band system-on-package," *IEEE Transactions on Microwave Theory and Techniques*, vol. 69, no. 9, pp. 4191–4198, 2021.

[16] Y. He, M. T. Craton, P. Chahal, and J. Papapolymerou, "A bi-material fully aerosol jet printed w-band quasi-yagi-uda antenna," in *2018 11th Global Symposium on Millimeter Waves (GSMM)*, 2018, pp. 1–3.

[17] D. Helena, A. Ramos, T. Varum, and J. N. Matos, "Antenna design using modern additive manufacturing technology: A review," *IEEE Access*, vol. 8, pp. 177 064–177 083, 2020.

[18] G. Ulisse, P. Schurch, E. Hepp, W. W. Koelmans, R. Doerner, and V. Krozer, "A 3-d printed helix for traveling-wave tubes," *IEEE Transactions on Electron Devices*, vol. 69, no. 11, pp. 6358–6361, 2022.

[19] CERES Printer Manual, Exaddon AG. [Online]. Available: https://documentation.exaddon.com/

[20] Z. Gao, M. Tang, P. Gao, H. Yue, and Y. Tang, "Design and measurement of d-band bonding-wire interconnection on quartz glass substrate," *2020 International Conference on Microwave and Millimeter Wave Technology (ICMMT)*, pp. 1–3, 2020.

Authorized licensed use limited to: Georgia Institute of Technology. Downloaded on August 12,2024 at 23:18:23 UTC from IEEE Xplore. Restrictions apply.